INTERFACIAL PATTERN FORMATION FAR FROM EQUILIBRIUM

E. Ben-Jacob[1,2], P. Garik[1,2], and D. Grier[1]

[1]Department of Physics
Randall Laboratory
University of Michigan
Ann Arbor, Michigan 48109

[2]Department of Condensed Matter Physics
School of Physics and Astronomy
Tel Aviv University
69978 Tel Aviv
Israel

(Received 19 May 1987)

Over the past few years diffusion-controlled systems have been shown to share a common set of interfacial morphologies. The singular nature of the microscopic dynamics of surface tension and kinetic growth far from equilibrium are critical to morphology selection, with special importance attributed to the anisotropy of these effects. The morphologies which develop can be organized via a morphology diagram according to the driving force and the effective anisotropy. We focus on the properties of the dense-branching morphology (DBM) which appears for sufficiently weak effective anisotropy, and the nature of morphology transitions between the DBM and dendritic growth stabilized by either surface tension or kinetic effects. The DBM is studied in the Hele-Shaw cell, and its structure analyzed by linear stability analysis. A comparison is made between the power spectrum of the structure and the stability analysis. We then provide a detailed account of the morphology diagram and morphology transitions in an anisotropic Hele-Shaw cell. Theoretically the question of morphology transitions is addressed within the boundary-layer model by computing selected velocities as a function of the undercooling for different values of the surface tension and the kinetic term. We argue that the fastest growing morphology is selected whether it is the DBM, surface tension dendrites, or kinetic dendrites. A comparison is made with our experimental results in electrochemical deposition for the correspondence between growth velocities and morphology transitions.

Over the past several years unifying principles governing the development of interfacial patterns have been arrived at after intensive study of theoretical models and experimental systems. It is now recognized that structures whose growth is diffusion-controlled share a common set of possible interfacial patterns and that a correspondence can be made between the control parameters which determine the selected morphology in these systems. Although simple scaling between systems may not be realizable, qualitative rules of morphology correspondence have been established by insightful identification of these control parameters. The macroscopic controls are self-evident, e.g., undercooling in solidification, supersaturation in precipitation, voltage drop in electrochemical deposition, or pressure differential in viscous fingering. The critical advance in understanding has been the discovery of the mathematically singular nature of the microscopic dynamics of crystalline anisotropy, growth kinetics, and surface tension[1-3]. Thus, it is now possible to speak broadly and say that when noise dominates the dynamics of the interface, the pattern which evolves has structure on many length scales, is likely to be fractal, and to resemble the computer generated diffusion-limited aggregation (DLA) morphology[4,5]; in the presence of surface tension and

0749-6036/87/060599+17 $02.00/0

either weak or vanishing anisotropy the evolved pattern is characterized by a dense-branching morphology (DBM) resulting from the repeated tip-splitting of advancing fingers[6]; faceted crystal growth develops for weak driving force and strong effective anisotropy; and, dendritic crystal growth can be stabilized by anisotropy in either the surface tension or the kinetics of attachment at higher driving force. It is to be emphasized that the control parameter regime of appearance of a morphology is the result of system dependent competition between microscopic and macroscopic dynamics producing "effective" surface tensions, anisotropies, and driving forces. Though the bulk of the research has been on two-dimensional systems, the extension to three-dimensions is in progress. For a given system these results are best summarized in a morphology diagram delineating the selected morphology as a function of the control parameters[3,7-10]. Such a diagram is reminiscent of a phase diagram. In what follows we will extend this analogy as we attempt to provide a first characterization of the nature of morphology transitions[11].

Part of the beauty of the field of interfacial pattern formation and morphology selection has been the complementary development of simple theoretical models and experimental systems to expose the underlying physics. At the outset, the first clear demonstrations of the singular nature of microscopic surface tension and anisotropy in morphology selection emerged from computer solutions of local models of solidification. Both the boundary-layer model[12] (BLM) and the geometrical model[13] demonstrated that anisotropy in either the surface tension or the growth kinetics is the singular perturbation required to stabilize dendritic growth in local models, while surface tension alone gives rise to tip-splitting growth. Also, it was in local models that the problem of dendritic growth velocity selection was first resolved[14,15]. Although these results have now been also achieved for the full nonlocal diffusion problem[16,17,18], the appeal of the local models remains two-fold: first there is their past success in including the correct fundamental physics; second, as was their initial attraction, the local models are computationally tractable. For these reasons, we have adopted the boundary-layer model for solidification as our testbed for morphology transitions. Below we find that within the BLM what we will call first- and second-order-like morphology transitions can occur depending upon the nature of the microscopic dynamics. Relying upon the morphology correspondence discussed above, and the prior predictive power of the BLM, we will then reason by analogy to understand such transitions in real systems.

The morphologies herein considered are experimentally observed on many length scales and in many different systems. Thus, in Fig. 1 the DBM which results when anisotropy is too weak to stabilize faceted or dendritic growth is shown on length scales varying from microns to decimeters. Similarly, in Fig. 2 we have dendrites on a comparable range of length scales. Though observable in a wide range of systems, the paradigmatic experiments selected to study morphology development are Hele-Shaw viscous fluid displacement[3,9,10,19-22] and electrochemical deposition[7,8,23]. Albeit a contrived system to demonstrate the importance of the "microscopic" dynamics of kinetic growth and surface tension in morphology selection, modified Hele-Shaw cells have proven a particularly lucid method to demonstrate the effects of anisotropy, and provided an important means to develop intuition as to the dominant effects in morphology determination. For this reason, our primary experiment to demonstrate morphology regimes and transitions in the body of this paper will be Hele-Shaw in a variety of modes. On the other hand, electrochemical deposition (ECD), though a less easily controlled system, is a true example of the results of the competition between microscopic dynamics and a macroscopic driving force. Variation of the anion employed enables the study of different microscopic anisotropy, kinetics and surface tension. Thus, the results from hexagonal Zn and fcc Cu show different morphologies at the same applied voltage, and the interplay of the macroscopic applied voltage and the microscopic dynamics has even been shown to give rise to a new metastable phase in Zn[8]. For these reasons we will also draw on our ECD results as support for our hypotheses.

In what follows we will focus on two related questions. First, we will present a study of the morphology which is observed to evolve in diffusion-controlled systems with weak or vanishing effective anisotropy: this is the DBM. We will review our earlier study of the DBM in the Hele-Shaw cell and the importance of kinetic effects in the dynamics of the interface of the DBM[6]. We further elaborate on our linear stability analysis of the DBM interface, and our hypothesis of the dominance of the fastest growing mode. In addition, we present new supporting evidence for our understanding of the DBM found by performing a power spectrum analysis of the structure. After this analysis of the DBM we will focus on morphology transitions in the Hele-Shaw cell in the presence of anisotropy. Details of the morphology diagram in Fig. 3 will be provided with an emphasis on the dynamics of growth, and the reappearance of apparent DBM growth between regimes of dendritic growth which are alternately stabilized by surface tension and kinetic effects. These experimental observations will then be examined within the BLM model in order to characterize the nature of the morphology transitions. This motivates our hypothesis that just as it is the fastest growing needle crystal which is the stable and selected

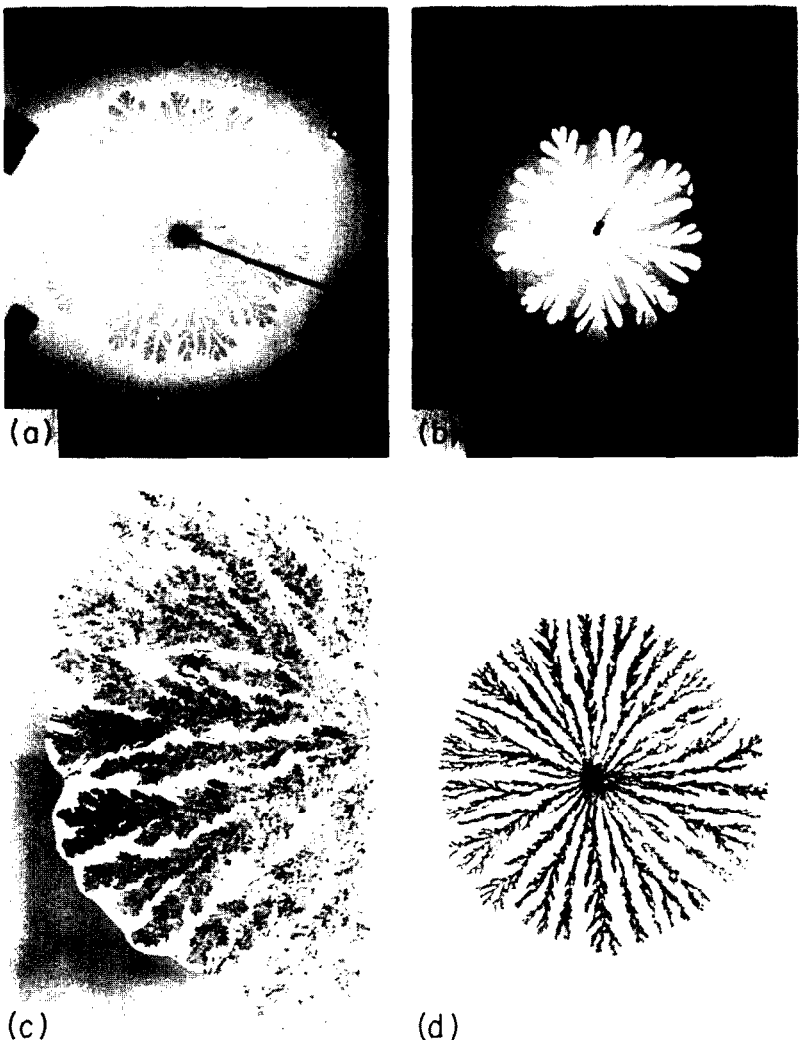

Fig. 1: The dense branching morphology as observed in several different systems. (a) The DBM generated in a Hele-Shaw cell by injecting water into glycerol. (b) Generation of the DBM by injection of oxygen at constant pressure into a Hele-Shaw cell filled with glycerol. The diameter of the cell in pictures (a) and (b) is 23". (c) The DBM as observed during annealing of $Al_{0.4}Ge_{0.6}$. The diameter is $\approx 30\mu$. (d) A DBM produced during electrodeposition in 0.4 M $CuSO_4$ at 7 Volts after 140 sec. The diameter of the electrodeposit is roughly 2 cm.

one, so more generally it is the fastest growing morphology which is selected. We have found that as in the case of phase transitions, morphology transitions in the BLM can be either continuous or discontinuous, as characterized by a continuous transition in the selected velocity of growth or a sudden jump in this velocity. Thus, the surface tension dendrites and kinetic dendrites observed in the Hele-Shaw experiment have analogues in the BLM. Finally, we speculate as to the implications this may have experimentally and present our new experimental evidence for the characterization of the morphology transition by the selected velocity in ECD experiments[11].

The Dense-Branching Morphology in the Hele-Shaw Cell

In the absence of sufficient anisotropy to produce dendritic growth repeated tip-splittings dominate the interfacial dynamics in diffusion-controlled

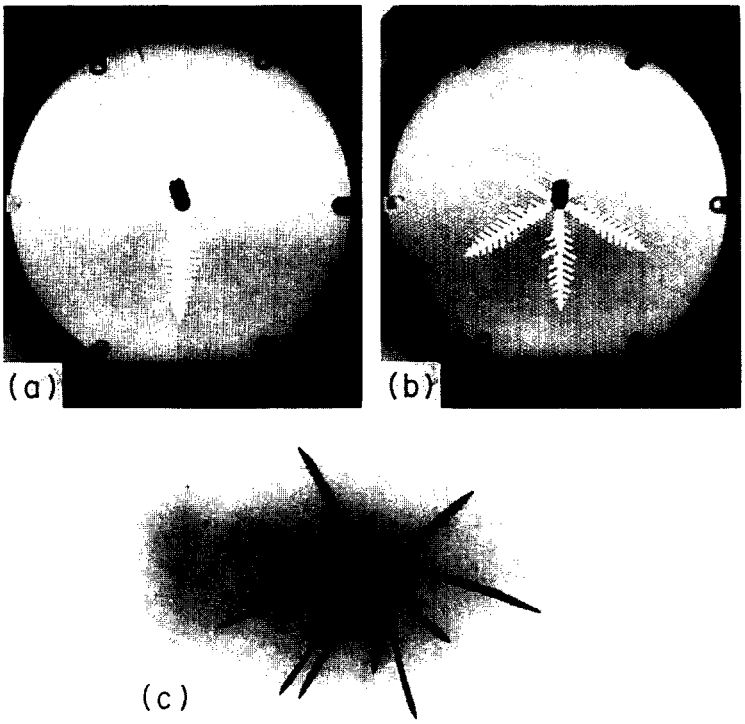

Fig. 2: Dendritic growths. (a) Dendrites in an anisotropic Hele-Shaw cell with four-fold symmetry. (b) Dendrites in an anisotropic Hele-Shaw cell with six-fold anisotropy. The length of a dendrite is $\approx$ 4 cm. (c) Dendrites in electrochemical deposition. The dendrite arms are roughly 1 cm in length.

growth. The result is a dense branching morphology (DBM) characterized by a circular envelope modulated by leading branch tips[6]. As shown in Fig. 1, the DBM is observed on length scales varying over six orders of magnitude in two dimensional systems. In addition to the examples displayed here, the DBM is observed in phospholipid solidification[24], Hele-Shaw in liquid crystals[10,22], and dielectric breakdown[25]. Moreover, it has now been argued that this morphology can be identified in three-dimensional systems such as spherulites[6,26].

The emergence of the dense branching morphology differs from a previous hypothesis[1,9] that tip-splitting dynamics would give rise to a fractal morphology like that obtained in simulations of diffusion-limited aggregation (DLA)[4]. This hypothesis had been found consistent with simulations of DLA with surface tension[27,28], a numerical solution to the Hele-Shaw equations[29], a deterministic algorithm for on-lattice aggregation[30], an experiment in a small radial Hele-Shaw cell[3], a Hele-Shaw experiment employing non-Newtonian fluids[21], and electrochemical deposition experiments[23,31]. By contrast, the dense branching morphology is not fractal: the lacunae do not scale with the size of the object and the DBM is of Euclidean dimension. However, our stability analysis[6,32] indicates that the initial branching rate of the DBM is similar to that of the DLA morphology. Based on the linear stability analysis presented below the DLA morphology identified in these systems can be viewed as the limit of the DBM for vanishing effective surface tension as defined below. This is the limit in which the branching rate of the DBM, as obtained from the stability analysis, reduces to that obtained earlier for DLA.

The Hele-Shaw experiment we performed to study the dense branching morphology was done in a cell with Paterson's radial geometry[19]. Recall that in general a Hele-Shaw cell is constructed so as to be able to inject a less viscous fluid into a more viscous one with the fluids forming a two-dimensional layer between two plates. In our experiment the plates were plexiglass with the upper one 3/4″ thick and 23″ in diameter; the lower plate was a square sheet 1″ thick. The two plates were flat to a tolerance of approximately 0.005″. The range of spacings betwen the

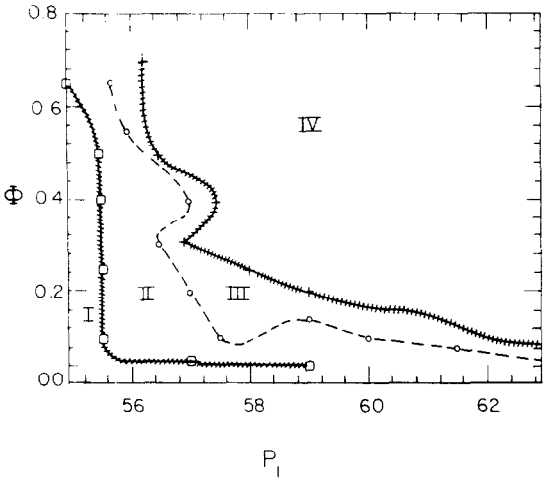

Fig. 3: Morphology diagram for a six-fold anistropic Hele-Shaw cell. Here P_1 is the applied pressure measured roughly in centimeters of Hg (the actual manometer fluid was a light oil). The anisotropy of the cell is measured by the ratio $\Phi = b_1/(b_0 + b_1)$ where b_1 is the depth of the grooves (0.015") and b_0 is the additional spacing between the top plate and the top of the grooved plate. The morphology regions are: I – faceted growth; II – surface tension dendritic growth; III – tip-splitting growth; IV – kinetic dendritic growth. Cross-hatching of curves separating labelled morphology regions indicates possible existence of narrow regions of other morphologies. E.g., as mentioned in the text between regions I and II there is evidence for DBM growth.

plates used was 0.4 - 0.8 mm. Our viscous fluid was pure ACS glycerol. We worked at a temperature of T = 22 ± 0.2°C with a corresponding viscosity, η, of the glycerol of 1200 centipoise. The less viscous fluids injected at the center of the cell were oxygen gas (at constant pressure) and water (constant flow rate). For the gas injection, the variation of pressure during the experiment was ≈ 2 mm of Hg. We repeated the experiment for pressures ranging from 50 to 150 mm of Hg. In order to avoid lifting of the plates (the applied force was up to ≈ 2000 nt) six 6" C-clamps were applied symmetrically around the boundary, and metal bars were clamped diametrically across the cell above and below each other. The same basic morphology was observed in all cases with the minimum length scale varying as a function of the spacing[33]. An example of the pattern is shown in Fig. 1(b). The stable circular envelope observed repeatedly developed even under less than perfect conditions.

When water was injected into the glycerol the same morphology developed. This experiment was performed at constant flow rates of the water ranging from 25 - 250 ml/min. Due to the miscibility of water and glycerol, there is no equilibrium surface tension but a dynamic interfacial tension resulting from a competition of the time scales for the advance of the interface and the diffusion rates between the two fluids. The effect of this reduced surface tension, as seen in a comparison of Figs. 1(a) and 1(b) is to produce a more open structure. The noisy bumps on the main stalks are also observed to be more pronounced than in the air into glycerol pattern.

As a first step in understanding the dense branching morphology, we did a linear stability analysis for the interface between the two fluids in analogy to a Mullins-Sekerka analysis[34]. A new element in our analysis was the inclusion of a kinetic term in the interfacial boundary condition. Such a kinetic term has proven important in explaining dendritic growth in solidification[14], and, as will be shown below, gives rise to dendritic growth distinct from that arising from surface tension alone in anisotropic Hele-Shaw experiments[11]. The Gibbs-Thomson relation including a kinetic term proportional to the normal velocity of the interface, v_n, is[6]:

$$p_s = p_1 - d_0\kappa - \beta v_n^{\gamma} \tag{1}$$

$$v_n = \frac{-b^2}{12\eta}\nabla p \cdot \hat{n} \tag{2}$$

where p_s the pressure in the fluid at the interface, p_1 is the pressure applied to the less viscous fluid , d_0 is twice the interfacial surface tension (for glycerol d_0 = 126 dyn/cm), κ is the curvature of the interface, $\hat{n}$ is unit normal to the interface in the direction of the more viscous fluid, and the pressure field $p(r,\theta)$ satisfies Laplace's equation. It has been shown[35] that under the assumption that Hele-Shaw flow occurs with a uniform wetting layer of fluid left by the receding more viscous fluid the exponent is $\gamma = 2/3$. In addition, for the case where the more viscous fluid is non-Newtonian γ appropriate to that fluid is expected[21]. For convenience, and also because we don't believe the precise value of the exponent is critical to the fundamental behavior of the interfacial development, in what follows we have taken $\gamma = 1.0$. In this case the time development of a perturbed envelope $R_s(\theta) = R + \delta_m \cos(m\theta)$ is given by:

$$\alpha_m(x) \equiv \frac{\dot{\delta}_m/\delta_m}{\dot{R}/R}$$

$$= -1 + m\left(x + \bar{\beta} - \frac{(m^2-1)(x\log_e(1/x) + \bar{\beta})}{\xi x - 1}\right)$$

$$\Big/\left(m\bar{\beta} + x\left(\frac{1-x^{2m}}{1+x^{2m}}\right)\right) \tag{3}$$

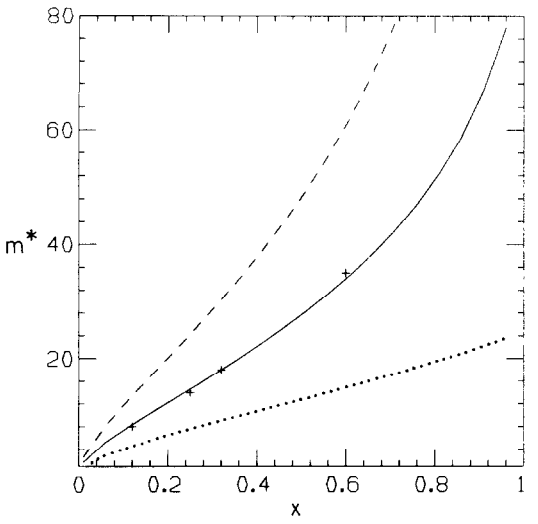

Fig. 4: Plots of the fastest growing mode as a function of x for different values of $\bar{\beta}$. The parameter $\xi = 1.6 \times 10^4$ as determined using $d_0 = 126$ dynes/cm, $b = 0.4$ mm, $R_0 = 23''$, and $p_g - p_0 = 50$ mm Hg. (—) is for $\bar{\beta} = 0.1$; $(\cdots)$ is for $\bar{\beta} = 1.0$; and $(- - - -)$ is for $\bar{\beta} = 0.01$. The $(+)$ points designate the number of experimentally counted main branches m_b for air into glycerol in an experiment with the above parameters. We estimate the value of $\bar{\beta}$ in this experiment to be ~ 0.1 using an heuristic argument. In the direction normal to the plates the viscous fluid front's profile can be approximated by a parabola. The fluid "left behind" the advancing parabolic tip is a narrow wetting layer. In order for this layer to advance as well, there must be an additional pressure drop on the fluid side of the interface. As an order of magnitude, estimate the width of this wetting layer as roughly 0.1 of the plate spacing. It follows that if the wetting layer is to move with the tip then $\bar{\beta} \sim 0.1$.

where $\xi = (p_g - p_0)/(d_0/R_0)$; $\bar{\beta} = \beta b^2/(12\eta R_0)$; and $x = R/R_0$. Here p_0 is the pressure at the radius R_0 (the radius of the cell), b is the plate spacing, and η is the viscosity. Implicit in such a stability analysis is that the interface is subject to a weak white noise, i.e., random fluctuations which do not swamp the microscopic dynamics of surface tension and kinetic effects. A study of (3) shows that there exists a fastest growing mode, $m^*(x)$, which maximizes α_m. We have proposed[6] that the observed number of major branches, m_b, can be approximated by $m^*(x)$. Our hypothesis is motivated by the results of the Rayleigh-Bénard and Couette-Taylor experiments where the selected wavelength, determined by nonlinear effects, is close to that of the fastest growing mode in the vicinity of the critical Reynolds number. Fig. 4 shows the agreement of the fastest growing mode hypothesis with results of our Hele-Shaw experiment. The value of m^* is determined by the interplay between the stabilizing effect of both the effective surface tension (i.e., ξ^{-1}) and kinetic terms, and the destabilizing effect of the diffusion field. In this context, the much greater branching observed in electrochemical deposition[7,8] corresponds to a substantially smaller effective surface tension. Similar such agreement with the fastest growing mode hypothesis has most recently been found in experiments using liquid crystals in a Hele-Shaw cell[22].

The results of the stability analysis can be tested further. The DBM interface shows substantially more structure than just that of "major" branches. There is additional modulation corresponding to slow variations in the interface, as well as finer structure corresponding to branch splitting. The relative rate of growth of perturbations that results from the linear stability analysis not only specifies the fastest growing mode, but also the relative rate of growth of other modes, as well as the high mode cutoff above which all modes are stable. That the branching rate as a function of the radius is indeed in accord with the linear stability analysis can be checked by taking the power spectrum of the DBM pattern, and comparing the observed modes and their relative magnitudes with the stability analysis. To measure the power spectrum of the branching rate we took a circular ring within the envelope of the interface, and digitized the density at this radius. Since the units of the power spectrum are arbitrary, we scaled it so that its maximum peak would be nearly (i.e., to within the accuracy of the abscissa digitization) the height of the fastest growing mode on the scale of α. As seen in Fig. 5, the result is that the linear stability analysis does indeed provide a useful prediction of the relative magnitudes of the observed modes, and a reliable high mode cutoff. The power spectrum measured for the full interface[20] is similar to that in Fig. 5. Our method of measuring the power spectrum of the branching suppressed low modes *ab initio*: a cut at a fixed radius necessarily eliminates long wavelength distortions of the entire structure. We have also done a crude power spectrum analysis of the entire envelope; in this the low modes $m < m^*$ re-emerged. Finally, the results of the power spectrum analysis justify after the fact the assumption of the weak, white noise made for the stability analysis[32].

Equation (2) can be further used to study the parameter regimes in which the branching structure of the DBM has previously been analyzed as a fractal object. For a fractal object the branching rate behaves like $\sim x^{D-1}$ where D is the fractal dimension. Although the DBM is not fractal, we can use $m^*(x)$ to compute an effective branching exponent:

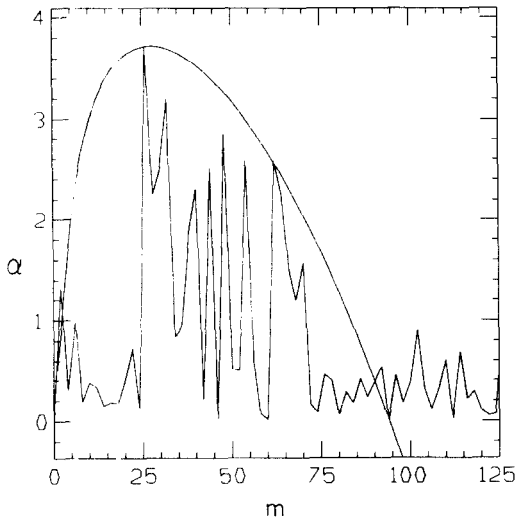

Fig. 5: Plot of the power spectrum described in the text for the DBM as measured at $x \approx 0.5$ with α as computed from equation (3) superimposed. Parameters are the same as in Fig. 4.

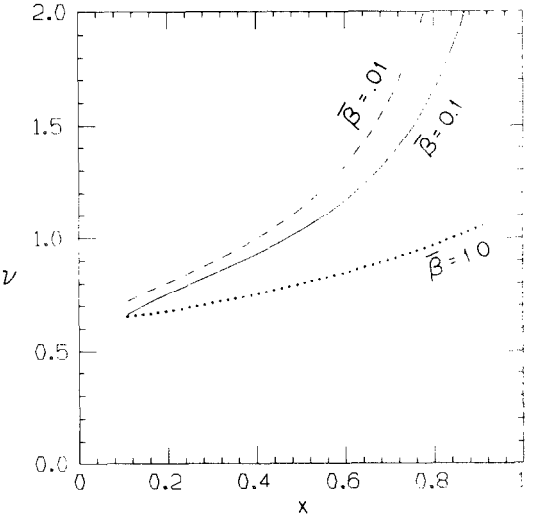

Fig. 6: Plot of $\nu = d\log m^*/d\log x$ vs. x for different values of the kinetic term. Parameters are the same as in Figs. 4 and 5. (—) is for $\bar{\beta} = 0.1$; (· · · ·) is for $\bar{\beta} = 1.0$; and (– – – –) is for $\bar{\beta} = 0.01$.

$\nu(x) \equiv d\log_e m^*/d\log_e x$. As shown in Fig. 6, for a wide range of parameters, for $x \approx 0.1$ (the definition of $\nu(x)$ is meaningless for smaller x), ν is approximately 0.7. Thus, in this range the DBM may display the mass distribution of the DLA morphology in both simulational and experimental studies. However, $\nu(x)$ increases with x and equals 1.0 for a value x_c. Regular branching in two dimensions is not possible for $\nu > 1.0$. At this crossover point we can speculate on the existence of a change in structure of the morphology. Predicting the nature of such a change is beyond the scope of linear stability analysis and requires a nonlinear study[32]. However, the point x_c can be calculated. Doing so we find that x_c depends very weakly on ξ and, for $0.05 \leq \beta \leq 0.5$, x_c ranges from 0.4 to 0.8. Finally, in the limit of vanishing effective surface tension ($d_0/R_0 \to 0$) $\xi \to \infty$ and $\alpha_m \sim (m-1)$; in this limit m^* diverges which according to our interpretation corresponds to the DLA limit in agreement with an earlier conjecture[36].

To conclude this section, we have shown that in diffusion-controlled systems with weak effective anisotropy the dense-branching morphology evolves in the Hele-Shaw cell. Appearing as it does in such a wide variety of systems, the DBM may be characterized as the complementary morphology to dendritic growth with the latter emerging in systems with larger effective anisotropy. Analysis of the Hele-Shaw experiment strongly suggests that the best way to characterize dense-branching growth is by m_b, the number of branches at a given radius; that the fastest growing mode found by a linear stability analysis is a good approximation to m_b; that the power spectrum displaying the branching rate is also in good agreement with this stability analysis; and that kinetic effects must be considered in determining the branching rate. Our analysis also suggests why the mass distribution of the DBM may be taken for that of the DLA morphology under certain experimental conditions, and is consistent with the evolution of DLA-like objects in the limit of vanishing effective surface tension.

Morphology Diagram for Anisotropic Hele-Shaw Flow

In the last section we studied interfacial development as determined by surface tension and kinetic effects, but in the absence of anisotropy. We now generalize this and study a Hele-Shaw system with both surface tension and kinetic anisotropies[11]. Moreover, in the experiment described below these anisotropies are in competing directions resulting in the particularly rich morphology diagram of Fig. 3. We find that the competitive anisotropies permit a morphology regime of tip-splitting, which is probably dense-branching growth, between dendrites which are stabilized alternately by surface tension anisotropy (STA) and kinetic anisotropy (KA).

The anisotropic Hele-Shaw experiments were performed in the same cell as described by Ben-Jacob et

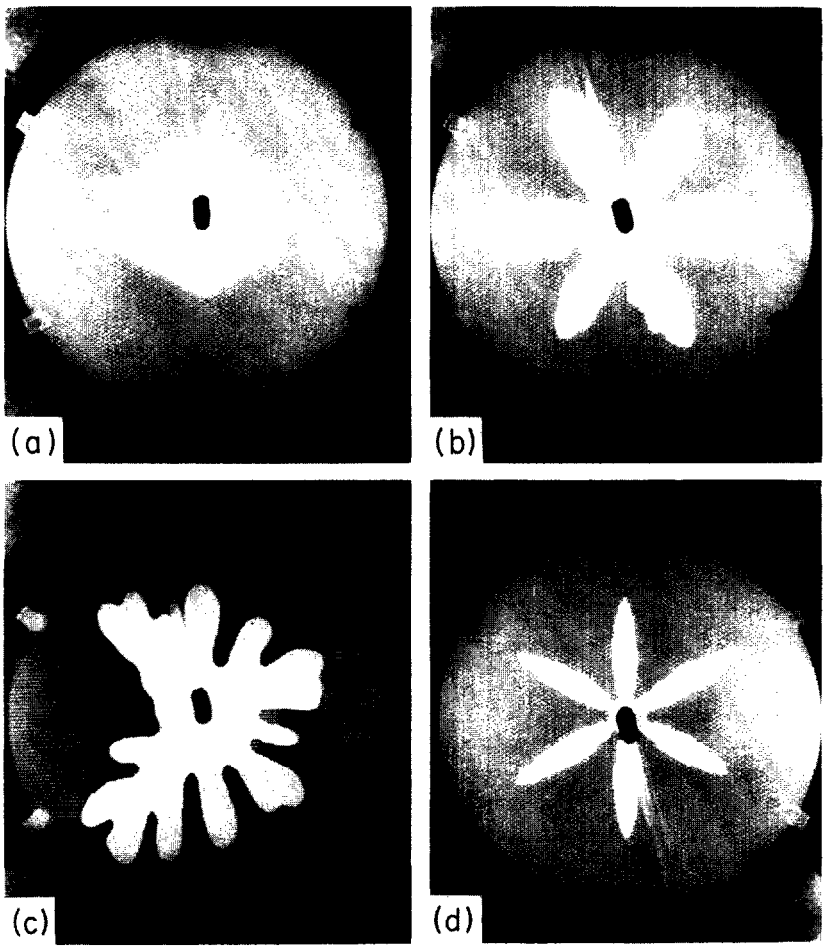

Fig. 7: Morphologies corresponding to the morphology diagram in the anisotropic Hele-Shaw cell. (a) Faceted growth. (b) Surface tension dendrites. With careful inspection it is possible to observe that the dendrite tips are pointed at an angle of 30° to the ruling of the grooves. (c) Tip-splitting growth. In a larger and more regular cell we assume that this would be a dense-branching growth. (d) Kinetic dendrites. The needle crystals grow parallel to the ruled channels.

al[3]. To review the experimental apparatus, air was pumped into glycerol which was used again as the viscous fluid. High purity glycerol (94%) dyed with food color was used. On the circular bottom plate, radius $R_0 = 25$ cm., was ruled a regular six-fold lattice of grooves with depth $b_1 = 0.015''$ and width $0.03''$. The effective anisotropy of the system, defined by $b_1/(b_0 + b_1)$, was varied by changing the spacing b_0 between the cell plates. The range for α in the experiments was between 0.1 and 1.0. Pressures ranging up to 100 mm of Hg were applied from a large (≈ 5 gallon) pressure reservoir.

The classification of the morphologies was made at the time when the average interfacial radius R was half the radius of the circular plate R_0. Specification of the radius at the point of classification is necessary since the pressure field in the glycerol satisfies the Laplace equation $\nabla^2 p = 0$. Thus, the effective driving force, proportional to $(p_{applied} - p_{atm})/R\log(R/R_0)$, increases with R with a consequent possible variation of morphology with time. In practice, this did not prove a problem in morphology identification. The morphologies observed, as a function of increasing applied pressure at a fixed effective anisotropy, are as follows.

At the lowest pressures applied faceted growth occurred (Fig. 7(a)). Flat interfaces that advanced a row at a time via nucleation and subsequent kink

propagation were observed. At slightly larger pressures both the nucleation time and the time for the propagation of a kink along the entire length of a facet become shorter, but with the nucleation time shorter than the propagation time. As a result, each face develops multiple propagating kinks. The upshot is an interface smooth on the scale of the interchannel spacing due to the overlap of the multiple kinks. However, the row by row advance is also sufficiently disturbed to produce roughness on a multiple channel scale. Characterization of this dynamic morphology requires a larger system. In this regime, between faceted and dendritic growth, tip-splitting is observed.

As the applied pressure is further increased the first transition to dendritic growth occurs. The underlying needle crystals point at a 30° angle to the direction of the lattice grooves (Fig. 7(b)). For reasons to be explained below, we designate these as surface tension anisotropy dendrites. With a continued increase of pressure the selected morphology once again becomes tip-splitting (Fig. 7(c)). Presumably this is the DBM however, due to the small size of our cell, relative to the cell dimensions the typical branch width is too large to produce the multiple tip-splitting necessary for a clear-cut identification. (On the other hand, in a demonstration cell with smaller interchannel spacing than in the experimental cell described above, it was possible to plainly identify a range of DBM growth after the surface tension dendrite regime.) Finally, at high driving force sixfold dendritic growth aligned with the channels occurs (Fig. 7(d)). These we refer to as kinetic dendrites. Between the DBM and kinetic dendrite regimes is a region in which the morphology is that of needle crystals without side-branches. Within the resolution of our measurements (pressure steps of 5 - 10 mm Hg) the transition to needles from either the DBM or kinetic dendrite sides is sharp. Nevertheless, at present we identify kinetic dendrites and undecorated needle crystal growth as the same morphology.

A qualitative understanding of the morphology diagram can be arrived at by considering the interfacial boundary condition, and the velocity field of the Hele-Shaw cell. Respectively these are:

$$p_s = p_1 - d(\theta)\kappa - \beta(\theta)v_n \tag{4}$$

$$v_n = \frac{-b(\theta)^2}{12\eta}\nabla p \cdot \hat{n} \tag{5}$$

which are of the same form as equations (1) and (2) except that now the plate spacing $b(\theta)$, the surface tension $d(\theta)$, and the kinetic factor $\beta(\theta)$ are all directionally dependent. It is the resultant angle dependent competition between the terms $d(\theta)\kappa$ and $\beta(\theta)v$ which gives rise to distinct kinetic and surface tension dendrites. By a simple energetics argument we can see that surface tension stabilizes dendrites at an angle of 30° to the channel grooves. This is because for a dendrite oriented in this direction the position of the interface is located where the effective distance between the plates is least thus minimizing the total surface area of the interface. Alternatively we can express this by saying that the increase in surface energy attendant to tip formation in a deep groove suppresses dendritic growth parallel to the grooves since this is the direction in which the interfacial area is maximized by the third dimension. On the other hand, as can be seen from equation (5), the larger b along the channels favors larger velocity in these directions. The result is that for large driving forces the resultant velocities are sufficient for the kinetic term to stabilize dendritic growth parallel to the channels. Thus the experimental observation that near equilibrium surface tension is dominant, whereas further from equilibrium it is kinetic effects that are most important in the stabilization of the needle crystal tip necessary for dendritic growth.

Additional qualitative morphological information is also indicated on the morphology diagram. At high applied pressure we observe stable dendrites whose stability is provided solely by the kinetic term in the boundary conditions. We emphasize that the shape of the morphologies which develop are sensitive to initial conditions. "Snowflakes" with 3, 6, or 12 branches are observed depending on the initial fastest growing mode of the circle. As further support that kinetic dendrites are due to the anisotropy in b, in 4-fold grooved cells the b^2 dependence of the interfacial velocity gives rise to slower dendrites growing at 45° to the main kinetic dendrites observed growing along the channels. Finally, in the absence of plate spacing ($b_0 = 0$) we are in the limit of zero surface tension (except within the channels). In this case, DLA-like structures are observed at low applied pressure consistent with the notion that DLA is a zero effective surface tension morphology, while at higher pressures dendritic-like or needle crystal-like structures appear depending on the channel widths[30,37].

Morphology Transitions in the Boundary-Layer Model

Motivated by our Hele-Shaw results, we now draw upon the analogy established between the effects of anisotropy in interfacial pattern formation in the Hele-Shaw cell, computer simulations, analytic solutions of the full solidification problem[16,17], and local models of solidification, and study the problem of the simultaneous effect of both surface tension and kinetic anisotropies in the boundary-layer model for solidification. The BLM is sufficiently tractable mathematically that it can be solved in the three regimes

found experimentally in anisotropic Hele-Shaw: surface tension anisotropy dominated dendritic growth, tip-splitting growth, and kinetic anisotropy dominated dendritic growth. The key feature which emerges from our analysis is that the velocity dependence on driving force of dendrites stabilized by surface tension is substantially different from that of dendrites stabilized by kinetic effects. This difference in scaling provides a qualitative explanation for morphology transitions which agrees with the Hele-Shaw morphology diagram, the results of our electrochemical deposition experiments, and previous experiments in crystallization from supersaturated solutions[38]. It further strongly suggests methods for more meaningful analysis of current solidification experiments. Preliminary results from a solution of the full model of solidification for the selected needle crystal velocities for either surface tension anisotropy or kinetic anisotropy alone are consistent with this difference in scaling between selected velocities indicating that again the local BLM has captured the fundamental physics of morphology selection. And again, the relative mathematical tractability of the BLM allowed us to study not only the selected velocity of the dendritic morphology, but also the time-dependent development of the selected needle-crystal to determine its stability as was necessary for our analysis.

For systems in which both surface tension and kinetic anisotropy are present there are two possibilities: either the directional preference of kinetic effects and surface tension are the same or they are in competing directions. Since crystalline anisotropy is the microscopic source of both anisotropies it is to be expected that in most systems surface tension and kinetic anisotropy are aligned. On the other hand, we have observed the dramatic effect that competing anisotropies have on the morphology diagram of the anisotropic Hele-Shaw cell. Thus, that there is evidence for kinetic anisotropy acting in competition with surface tension anisotropy far from equilibrium in other systems is of great interest. In experiments of dendritic growth from supersaturated solutions Chan[38] et al have observed substantial variation of the tip velocity and selected crystalline growth direction with increasing supersaturation. The results of this section will make it plausible that these observations are consistent with the competition between surface tension and kinetic anisotropies as observed in anisotropic Hele-Shaw, although we further recognize that in three-dimensional crystallization there is the additional complication of competition between different kinetic anisotropies. With this physical motivation we now study the selected needle crystal velocities for both aligned and competing anisotropies.

The boundary conditions for solidification are very similar to those for anisotropic Hele-Shaw. The velocity of interfacial advance, V_n, is determined from the equation of continuity for the heat generated at the interface during solidification and then diffused into the melt. (In the one-sided model adopted here diffusion of heat in the solid is ignored.) With the material constants L, the latent heat of fusion, D, the thermal diffusion coefficient, C_p, the specific heat at constant pressure, and $\hat{n}$ the interface normal directed towards the melt, the normal velocity V_n of the interface satisfies[1]:

$$LV_n = -DC_p(\nabla T \cdot \hat{n})_s \tag{6}$$

We now assume that far from the growing solid the temperature of the melt is $T_\infty < T_M$ with T_M the melting temperature. The temperature equivalent of equation (5) is then the Gibbs-Thomson relationship with kinetic term describing the temperature distribution at the interface between melt and solid:

$$T_s = T_M - \frac{L}{C_p}d(\theta)K - \frac{L}{C_p}\beta(\theta)V_n \tag{7}$$

where T_s is the temperature at the interface surface, K its curvature, and the angular dependences of the surface tension and the kinetic term are:

$$d(\theta) = d_0(1 - d_1 \cos m(\theta - \theta_d))$$

$$\beta(\theta) = \beta_0(1 - \beta_1 \cos m(\theta - \theta_\beta)).$$

Here d_0 is the capillary length; the isotropic kinetic coefficient is β_0; d_1 and β_1 are dimensionless measures of the degree of the two anisotropies; m is the symmetry of the anisotropy; and, θ_d and θ_β are offset angles from the $\hat{y}$ axis for surface tension and kinetic effects respectively. A dimensional analysis of β_0 suggests that it is useful to think of it as ${d_0}^{-1}\Omega^{-1}$ with Ω a characteristic frequency for kinetic attachment.

Solution of the full solidification problem would require solution of the diffusion equation $\frac{\partial T}{\partial t} = \nabla^2 T$ with equations (6) and (7). By instead adopting the boundary-layer model, we make the approximation that within a decay length l, the boundary-layer, the temperature field at the interface becomes T_∞. In terms of the undercooling $\Delta = C_p(T_M - T_\infty)/L$, this approximation is in principle valid only in the high undercooling limit, $\Delta \approx 1$. The BLM variable of interest is H, the heat content per unit interfacial length (or per unit area in three dimensions), defined as:

$$H(S,t) = \int_0^\infty dz\, C_p(T(S,z) - T_\infty)$$

where the integration variable z is the distance away from the surface measured along $\hat{n}$ and S is the arclength variable for the interface. This provides an

expression for the length l as $H = C_p(T_s - T_\infty)l$. In two dimensions the time evolution of the field H is given as the sum of the latent heat generated, the heat necessary to bring the new portion of solid up to the temperature T_s from T_∞, the diffusion of heat along the interface, and a geometrical term resulting from the local change in arclength:

$$\left.\frac{dH(S,t)}{dt}\right|_n = V_n(L - C_p(T_s - T_\infty)) + D\frac{\partial}{\partial S}(l\frac{\partial T_s}{\partial S}) - KV_nH \qquad (8)$$

where S and t are the arclength coordinate and time respectively. As time develops each interfacial point moves along the normal to the surface with velocity V_n. The notation $|_n$ refers to the fact that the derivative is evaluated using the infinitesimal difference dH as evaluated along this normal. This equation must be coupled with the equations describing the geometrical evolution of the interface. Defining $\hat{t}$ and $\hat{n}$ as the unit tangent and unit normal at a point on the interface, our sign conventions are that $\hat{t} \times \hat{n}$ is normal to the page, $\hat{n}$ is the outward normal of the interface, and with the orientation of $\hat{n}$ specified by its angle θ relative to a fixed direction (typically the standard $\hat{y}$ direction in the xy-plane), we define the curvature K by $\frac{d\hat{t}}{dS} = -K\hat{n}$. From this follows $\frac{d\theta}{dS} = K$. Now let $\vec{r}(u,t)$ be the position of the interface as parametrized by u which is time independent. By definition $\frac{d\vec{r}}{dt} = \hat{n}V_n$ defines the interfacial advance. Then it can be shown that:

$$\frac{dS}{dt} = \int_0^S dS'\, K(S',t)V_n(S',t) \qquad (9)$$

$$\left.\frac{dK(S(t),t)}{dt}\right|_n = -(\frac{\partial^2}{\partial S^2} + K^2)V_n. \qquad (10)$$

[For more details on this differential geometry see Ref. 13.] These equations, coupled with the equation (8), completely define the time evolution of the interface and can be solved numerically. It was by this means that the first demonstration that anisotropy is required for dendritic growth was accomplished: with anisotropy these coupled equations produce a dendritic interface; in the absence of anisotropy a tip-splitting interface evolves from these equations[1].

Experimentally observed dendrites possess an underlying parabolic shape if shorn of their side-branches. This shape, called the needle-crystal, is preserved in time as the tip of the dendrite advances at what appears to be a uniform velocity. It suggests that a stationary solution to the solidification equations exists in a frame of reference moving with the needle-crystal. Of course, this cannot be a stationary frame for the complete dendrite; in such a moving frame a dendrite must appear as a needle-crystal decorated with a train of side-branches which begin growing near the tip and then propagate backwards along the trunk of the needle. Nevertheless, consideration of the existence and stability of the needle-crystal is a logical first step since its properties, especially the selected velocity, are close to those of the full dendrite. For the full solidification problem it is well-known that for the interfacial boundary condition $T_s = T_M$ such needle-crystal solutions exist. In two dimensions these Ivantsov needle crystals[39,40] are parabolas such that for given undercooling specifying either the tip radius or the tip velocity fixes the other quantity, but a specific parabola is not selected by specifying the undercooling alone. Part of the close correspondence between the boundary-layer model and the full solidification problem is that for the interfacial boundary condition of an isotherm at the melting temperature the BLM also possesses a set of parabolic Ivantsov solutions[1]. These solutions are

$$K = \frac{V_0}{D}\frac{(1-\Delta)}{\Delta^2}\cos^3\theta$$

where V_0 is the velocity of the tip.

For many years an outstanding problem in pattern selection was how to determine the tip velocity or radius of the physically selected needle-crystal, a solution expected to correspond closely to the dendritic solution. Resolution of this problem was first achieved in the local models via the "microscopic solvability criterion"[12,13]; this method has subsequently been extended to the full solidification problem[16]. In the BLM the first step is to change reference frames to the moving frame of the presumed needle-crystal. Assume that the needle-crystal tip is advancing with a constant velocity V_0. Directly from the definition of the normal velocity of the interface, it follows that if each point on the interface advances parallel to the direction of the tip with velocity V_0 then $V_n(S) = V_0\cos\theta(S)$. Moreover, in the moving frame we have $\frac{\partial H(S,t)}{\partial t} = 0$ and $\frac{\partial K(S,t)}{\partial t} = 0$. Thus, using equations (8) and (10), in the moving frame the needle crystal is defined by:

$$V_n(L - C_p(T_s - T_\infty)) + D\frac{\partial}{\partial s}(l\frac{\partial T_s}{\partial s}) - KV_nH - \frac{\partial H}{\partial S}\frac{dS}{dt} = 0 \qquad (11)$$

$$\frac{\partial K(S(t),t)}{\partial S}\frac{dS}{dt} + (\frac{\partial^2}{\partial S^2} + K^2)V_n = 0. \qquad (12)$$

Equation (12) with the moving frame expression for V_n can be used to eliminate $\frac{dS}{dt}$ from equation (11).

This then allows equation (11) to be written as three first order coupled nonlinear differential equations. For the numerical computation scheme it is useful to introduce dimensionless fields as follows[1]:

$$h = \frac{\Delta^3 H/L}{d_0}; \quad \kappa = \frac{d_0 K}{\Delta^3}; \quad s = \frac{\Delta^3 S}{d_0}; \quad v_n = \frac{d_0 V_n}{D\Delta^5};$$

and $u = C_p(T_s(s,t) - T_\infty)/L$. In terms of these fields equation (11) can be expressed as the system[12]:

$$\frac{d\theta}{ds} = \frac{1}{\Delta^2 d(\theta)/d_0}\left(1 - \frac{u}{\Delta} - \Delta^4 \frac{D}{d_0}\beta(\theta) v_0 \cos\theta\right) = \kappa \tag{13}$$

$$\frac{du}{ds} = \lambda \tag{14}$$

$$\frac{d\lambda}{ds} = 2\Delta^2 \lambda v_0 \sin\theta + \Delta^2 v_0 \kappa u \sec\theta - \Delta^4 {v_0}^2 \cos^2\theta \frac{1-u}{u} - \frac{\lambda^2}{u} - \lambda\kappa\tan\theta. \tag{15}$$

With initial conditions equations (13), (14), and (15) define a nonlinear eigenvalue problem for the selected velocity of the needle-crystal. The problem is posed in terms of the value of $\lambda(0)$. For a needle-crystal solution to these equations to exist u, the dimensionless temperature at the surface, must be symmetric about the origin. This requires that $\lambda(0) = 0$. For given parameters (i.e., Δ, d_1, β_0, and β_1) an eigenvalue v_0 is now determined by integrating the equations from the initial conditions at $\theta = \pi/2$ (i.e., $s \to \infty$ back to $\theta = 0$ (i.e., $s = 0$) for a trial v_0. If $\lambda(0)$, the so-called mismatch function, vanishes then the velocity eigenvalue, the selected velocity v^* has been found. As a practical numerical matter, the mismatch function never completely vanishes. However, one can integrate the equations from the initial conditions to $s = 0$ ("shoot backwards") and find the range of v_0 over which $\lambda(0)$ changes sign. The selected velocity eigenvalue v^* is then determined by interpolation. It is also possible for there to be more than one value of v_0 such that $\lambda(0) = 0$. In this case it is the largest v_0 determined which corresponds to v^*[12]. This method of determining v^* constitutes the microscopic solvability condition as applied to the BLM.

It remains to specify the initial conditions for these equations. This is accomplished by observing that equations (13)–(15) possess fixed points at $\theta = \pm\pi/2$ (i.e., $s = \pm\infty$). It can be shown[1,12] that there is only one trajectory leading into these fixed points, and that this trajectory is asymptotically identical to the equivalent Ivantsov trajectory. Since at $\theta = \pm\pi/2$ the needle crystal is expected to have vanishing curvature and normal velocity, the Ivantsov solution *with the specified needle-crystal velocity* is asymptotically a better and better approximation to the needle-crystal solution. In principle this provides the initial conditions of the Ivantsov solution at $\theta = \pi/2$ with $\kappa(\frac{\pi}{2}) = 0$, $\lambda(\frac{\pi}{2}) = 0$. In practice, integrating over arclength from $\theta = \pi/2$ corresponds to an infinite integral, so we take as large an initial θ as numerically feasible and evaluate the Ivantsov solution at that point to obtain the initial conditions for the shooting. Typically $\theta \approx 1.4$ is chosen and the value obtained then checked at $\theta \approx 1.45$ or 1.50 for convergence.

A precise comparison of the effects of surface tension and kinetic anisotropy on the value of V^* for a given system requires knowledge of the parameters d_0, d_1, β_0, and β_1. Nevertheless, a qualitative understanding of their possible relative importance can be developed. In Fig. 8 selected velocities as a function of undercooling Δ are plotted for the case of sixfold symmetry and a range of surface tension and kinetic parameters with kinetic anisotropy and surface tension anisotropy alternately neglected in Figs. 8(a) and 8(b). Although in the limit of vanishing Peclet number ($\Delta \to 0$) the selected velocity $V^* \sim \Delta^4$, the log-log presentation of the higher undercooling regime studied here shows that surface tension anisotropy and kinetic anisotropy give rise to V^* scaling with Δ with a rough difference in exponents of ≈ 3. The parameter regime chosen is such that there is a significant overlap in V^* between the two cases. A comparison of Figs. 8(a) and 8(b) shows that while at low undercooling surface tension anisotropy selects larger V^* than kinetic anisotropy, the larger exponent for kinetic anisotropy determined V^* results in this reversing at larger Δ. Thus, in systems where both surface tension and kinetic effects are of the same order of magnitude, at low driving force STA will be dominant in determining the selected velocity, whereas at high driving force V^* will be predominantly determined by kinetic effects. For intermediate driving forces whether the two anisotropies are aligned or competing will be critical to the value of the selected morphology and V^*. This scenario corresponds precisely to what our anisotropic Hele-Shaw observations. Moreover, as one would hope, the conclusions drawn above from the local BLM are now supported by preliminary work solving the full diffusion problem. Our initial numeric studies of the dependence of V^* shows roughly the same difference in scaling as a function of undercooling between surface tension and kinetic anisotropies. For this reason, we expect that the analogues of Figs. 8 and 9 will be obtained for the full diffusion equation.

As sketched, the different undercooling dependence of V^* for STA and KA stabilized dendrites has important implications for morphological transitions. For a particular set of parameters, Fig. 9 is a study of the selected needle crystal velocity for the two different cases of aligned and competing anisotropies. For

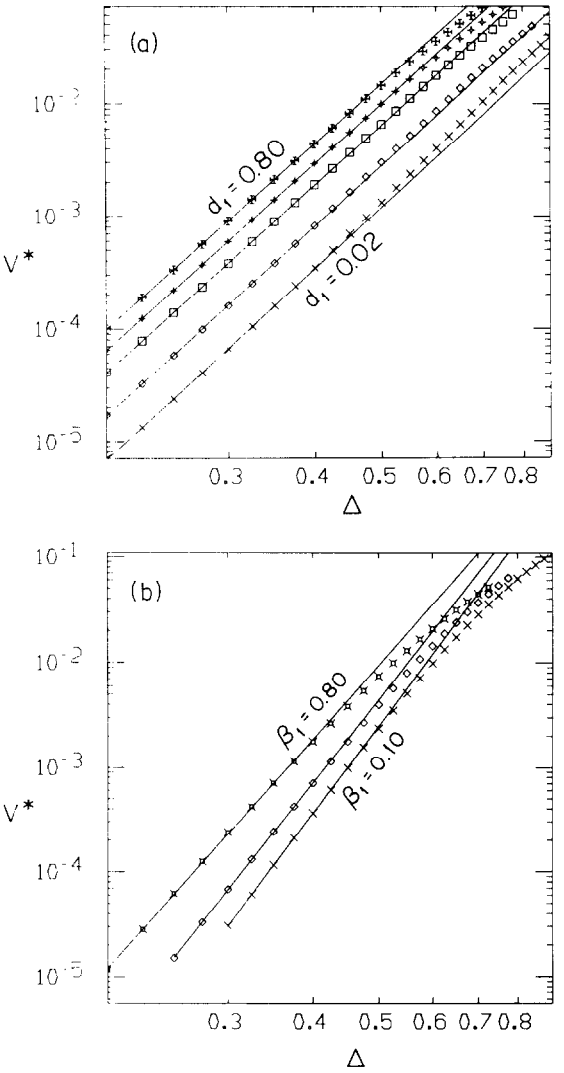

Fig. 8: Log-log plots of the selected velocity V^* as a function of the undercooling Δ in the BLM for different values of the anisotropy. Here V^* is measured in units of D/d_0. The straight lines through the computed values of V^* are least squares fits. The fits were done over the range $0.2 < \Delta < 0.4$. (a)Surface tension anisotropy selected velocities computed for different values of d_1 ($d_0 = 1.0, \beta_0 = 1.0, \beta_1 = 0$). Beginning with the lowermost set of data points the values of d_1 are 0.02, 0.06, 0.20, 0.40, and 0.80. The bracketing values of the best fits are for $d_1 = 0.02, V^* \sim \Delta^{5.64}$ and for $d_1 = 0.80, V^* \sim \Delta^{5.47}$. (b) Kinetic anistropy selected velocities computed for different values of β_1 ($d_0 = 1.0, d_1 = 0.0, \beta_0 = 1.0$). Beginning with the lowermost set of data points the values of β_1 are 0.10, 0.20, and 0.80. The bracketing values of the best fits are for $\beta_1 = 0.10, V^* \sim \Delta^{8.61}$ and for $\beta_1 = 0.80, V^* \sim \Delta^{7.26}$

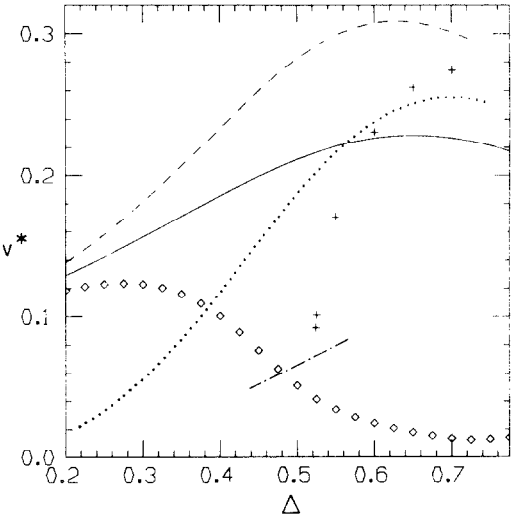

Fig. 9: Aligned and competing anisotropies for $\beta_0 = 1.0, \beta_1 = 0.4, d_0 = 1.0$, and $d_1 = 0.20$. The scaled velocity $v^* = \frac{d_0 V_n}{D\Delta^5}$ is plotted vs. Δ. (– – – –)is for aligned anisotropies ($\theta_\beta = \theta_d = 0$). (—) is for surface tension anisotropy alone ($d_0 = \beta_0 = 1$, $\beta_1 = 0$, and $d_1 = 0.20$). (· · · ·) is for kinetic anisotropy alone ($d_0 = \beta_0 = 1$, $d_1 = 0$, and $\beta_1 = 0.40$). ($\diamond$) – v^* as determined assuming a surface tension needle crystal ($\theta_d = 0$ and $\theta_\beta = 0.5236$. (+) – v^* as determined assuming a kinetic needle crystal ($\theta_d = 0.5236$ and $\theta_{beta} = 0$. Curve (– – – · – – – · – – –) is our hypothesized v^* for the tip-splitting DBM interface found between the surface tension and kinetic anistropy regimes. Numerical solution of the BLM for the development of the interface in time shows that at $\Delta = 0.45$ the needle crystal evolves into a dendrite, while at $\Delta = 0.475$ the needle crystal is unstable and tip-splitting growth occurs. [N.B.: A slightly different form of the surface tension anisotropy was used for the computations of v^* than that presented in the text. Computations were done with: $d(\theta) = d_0(1 - d_1 \cos m(\theta - \theta_d))/(d_0 + d_1)$.]

aligned anisotropies, there is a crossover in the slope of $\log V^*$ vs. $\log \Delta$ around $\Delta = 0.56$. This is the shift in the source of the needle crystal stabilization from surface tension to kinetic stabilization. By analogy to the Hele-Shaw case, we refer to this as the transition between surface tension dendrites and kinetic dendrites. Although the selected morphology remains dendritic throughout this range of parameters, as we have verified by studying the time dependent evolution of the selected needle crystal, the underlying physics has changed with implications for dendritic

single crystal growth in real systems. Moreover, such a crossover in the slope of the velocity should be experimentally verifiable.

For the case of competing anisotropies the question arises as to the interpretation of the direction of the needle crystal tip. Competing anisotropies mean that θ_d and θ_β are unequal. On physical grounds, and justified by our simulations, we can choose one of them as zero. This is tantamount to assuming that the needle-crystal is stabilized either by surface tension anisotropy ($\theta_d = 0$) or by kinetic anisotropy ($\theta_\beta = 0$), and is not oriented somewhere in between. Needle crystals stabilized in the former fashion we designate as surface tension needle crystals, those stabililzed in the latter manner are kinetic needle crystals. Selected velocities are now sought for given Δ with either orientation, i.e., either $\theta_d = 0$ or $\theta_\beta = 0$. As seen in Fig. 9 this leads to the possibility of two selected velocities for the same undercooling. In particular, selected velocities for surface tension dendrites exist in the undercooling regime where the kinetic needle crystal velocity is greater. What we find is that in this case the smaller velocity corresponds to an unstable solution which tip-splits when allowed to develop in time.

With this understanding of the needle crystal in the presence of anisotropies, we now consider the case of six-fold anisotropy but with the surface tension and kinetic anisotropies offset by 30°. As seen in Fig. 9, the result is that in the region where the two anisotropies are of comparable strengths, as judged by the fact that either alone would produce the same selected velocity, the selected velocity shows first a precipitous decline producing a "gap" in which the selected needle crystal is unstable (as determined from its time-dependent evolution), and then a sudden increase. To the accuracy of our computations we find that starting from a surface tension stabilized tip there is always a selected velocity over a broad range of undercooling. However, as observed above, in the region of undercooling in which we show two values of v^* the smaller v^* is unstable and tip-splits as determined by the time dependent evolution of the needle crystal. By contrast, there is a minimum value of Δ such that below this value there is no selected velocity for kinetic anisotropy stabilized needle crystals.

Our interpretation of Fig. 9 is that after a regime of surface tension dendrites at moderate undercooling, the competition between the two anisotropies opens a region of tip-splitting, and dense-branching growth. By analogy to the selection rule for dendrites that the fastest growing needle crystal is the selected one, we now generalize and say that it is the fastest growing morphology which is the selected. Thus, in this gap between dendrites we have sketched a hypothetical curve for the selected velocity for DBM growth. The behavior of the v^* transition between surface tension dendrites and the DBM, and the transition between the DBM and kinetic dendritic growth lead us to draw an analogy between these morphology transitions and a thermodynamic phase transitions. We suggest that the transition from surface tension dendritic growth to DBM growth is analogous to a second order phase transition: we expect the selected velocity to be continuous as a function of undercooling, but to show a discontinuity in its slope. In keeping with this analogy, the transition from DBM growth to kinetic dendrites may be first order if there is a jump in v^*. It is at least a second-order like transition since from the kinetic stabilized side of the slope of the v^* diverges at the reentrant transition from tip-splitting to dendritic growth.

Experimental Morphology Transitions and Electrochemical Deposition

In the last section we provided a qualitative understanding for the observed morphology transitions in the anisotropic Hele-Shaw cell by studying the correspondence between the selected interfacial velocity and the selected morphology in a model for solidification. Although there is a dearth of experimental examples of measurement of the velocity of growth as a function of driving force, we now briefly consider two other examples of which we are aware: our own experiments in electrochemical deposition and the data of Chan et al[38] for the case of supersaturated solutions.

Chan et al report that during crystallization from a supersaturated NH_4Cl solution both the velocity of the observed dendrites and the crystal face presented by the growing dendrites varies with the supersaturation. The measure of supersaturation was the dimensionless quantity $\Pi = (c_\infty - c_0)/c_0$ where c_∞ is the NH_4Cl solution interface of a NH_4Cl crystal. Four regimes of growth were reported:

1. For $0.0 < \Pi < 0.08$ dendrites with the $< 100 >$ crystal face orientation were observed to grow with a velocity increasing to $\approx 50\,\mu$/sec.
2. For $0.08 < \Pi < 0.15$ the growth is tip-splitting dendritic, i.e., the advancing dendritic tip splits spawns two $< 100 >$ dendrites, one of which eventually overwhelms the other. The velocity in this regime is constant at $\approx 50\,\mu$/sec. Onset of the unstable growth is reported to be marked by a kink in the V vs. Π plot.
3. Subsequent to dendritic tip-splitting growth, over the range $0.15 < \Pi < 0.22$ dendrites with $< 110 >$ crystal face orientation grow. The velocity gradually increases to $120\,\mu$/sec.
4. At $\Pi \approx 0.22$ there is a discontinuous jump in the growth velocity as dendritic growth with $< 111 >$ orientation begins. The jump is from $120\,\mu$/sec to

$800\,\mu$/sec. By comparison to the lower Π regimes after the jump the velocity increases rapidly appearing linear in Π with a slope of $2400\,\mu$/sec.

In the language developed in the sections above, it appears that the competition between $< 100 >$ and $< 110 >$ growth give rise to the unstable dendritic tip-splitting growth *although Chan et al do not report* $< 110 >$ *growth in this regime.* Unlike the Hele-Shaw case and the BLM competing anisotropy simulation, it appears that for crystallization of NH_4Cl the effective anisotropy is too strong to admit DBM tip-splitting growth. However, the observed discontinuity in the slope of velocity vs. supersaturation suggests what we would designate a first-order morphology transition between the stable $< 100 >$ dendritic growth and dendritic tip-splitting. In passing we note that we too have observed such unstable dendritic tip-splitting growth during electrochemical deposition experiments in a capillary tube[40]. The fact that the transition from dendritic tip-splitting to $< 110 >$ growth is accompanied by at most a weak discontinuity suggests strongly to us that in the tip-splitting regime both $< 100 >$ and $< 110 >$ dendrites should be observed, at least close to the transition supersaturation $\Pi = 0.15$. Finally, the abrupt jump transition between $< 110 >$ and $< 111 >$ growth with the accompanying dramatic change in slope strongly resembles the first-order morphology transition for the onset of kinetic anisotropy growth shown in Fig. 9 although in this case the transition is due to competition between kinetic anisotropies. The greater variety of possible effects due to crystalline anisotropy in three-dimensions emphasizes the limitiations of the two-dimensional BLM results. Nevertheless, it appears that many of the characteristics of crystallization from supersaturated solutions fit into the framework of morphology transitions we have sketched.

We now discuss our own measurements of interfacial velocity and morphology transitions made during growth by electrochemical deposition. The experimental apparatus is a refinement of that reported in Grier et al[8]. The diameter of the outer Cu ring electrode is 8.0 cm and the electrolyte is $ZnSO_4$. In electrochemical deposition the driving force is the applied voltage, however the concentration of the electrolyte is also variable. This allows a study of the interface velocity and morphology transitions as a function of both concentration and applied field. Fig. 10 shows the transition in the velocity of interfacial advance between dense-branching and dendritic growth for two different molarities of $ZnSO_4$ solution. Measurements of the velocity were made at a radius of 1.0 cm, i.e., in the notation of the DBM section, at $x = 0.25$. There is a clear change in slope for v vs. V at the transition from DBM growth to dendritic growth. For these low concentrations the transition is very sharp

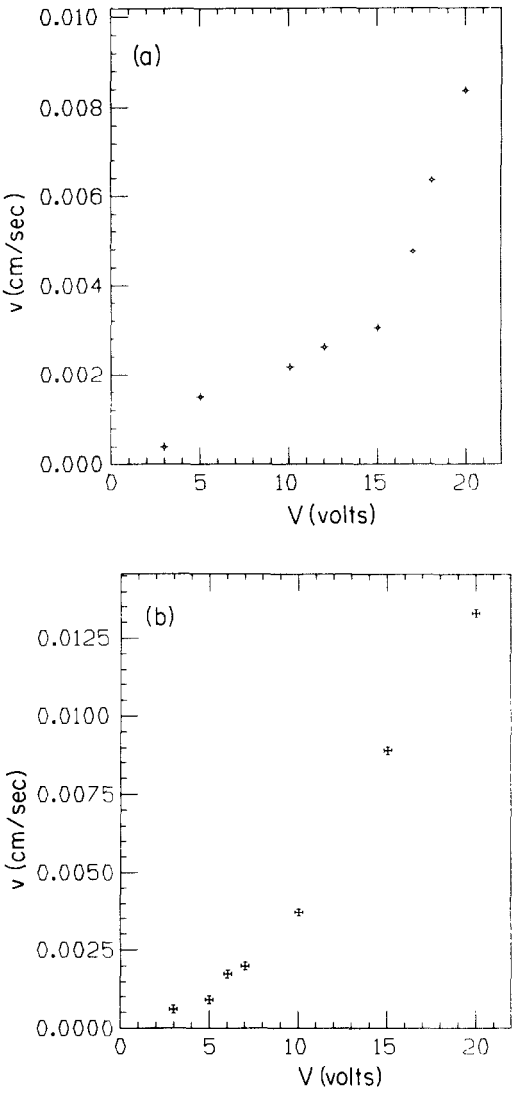

Fig. 10: Plots of the velocity of interfacial growth in electrochemical deposition. Velocities were measured at $x = 0.25$, i.e., at 1/4 the cell radius. (a) ECD in 0.05M $ZnSO_4$ solution. Dense-branching growth is observed for voltages < 12 volts, and dendritic growth for voltages > 15 volts. (b) Corresponding plot for $0.10M$ $ZnSO_4$ solution.

and in qualitative agreement with Fig. 9. At higher concentrations the transition becomes more gradual. In Fig. 11 we show the two morphologies at 0.05M. Both are examples of stable envelope growth, however Fig. 11(a) is a tip-splitting DBM while Fig. 11(b) is composed of dendrites. Further details and analysis of these results will be presented in Ref. 11.

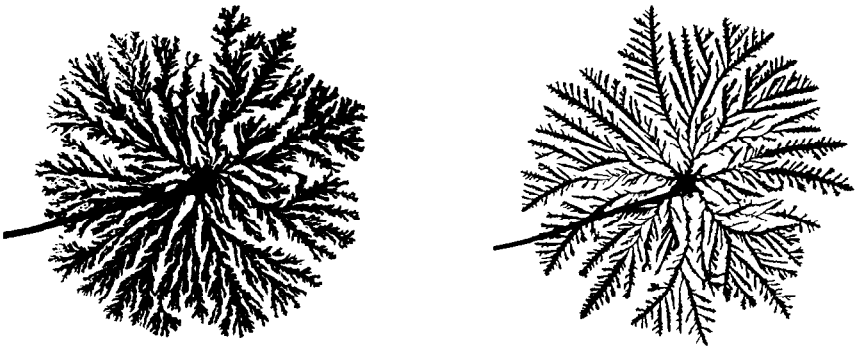

Fig. 11: Morphologies as observed in 0.05M $ZnSO_4$ solution. (a) DBM at 4.06 Volts. (b) Dendritic growth at 20.0 Volts.

Conclusions

In the above sections we have examined the problem of morphology transitions in diffusion-controlled systems. We have shown that morphology transitions in the boundary-layer model may be either continuous or discontinuous as characterized by the selected needle crystal velocity. For the case of competing anisotropies we have further found that tip-splitting growth may arise as a result of competition between surface tension and kinetic anisotropies. Throughout we developed intuition and drew strong support for our theoretical model of morphology transitions and by making comparison to our anisotropic Hele-Shaw and electrochemical deposition experiments. The work presented here is at best a first preliminary attempt to characterize morphology transitions quantitatively. Much theoretical and experimental research remains to be done. In particular, more emphasis must be devoted to microscopic material transitions which accompany the macroscopic interfacial morphology transitions we emphasized here. Such have already been reported in electrochemical deposition[8]. Generally we expect that the mathematically singular nature of the microscopic dynamics which emerges theoretically must translate into experimentally observable microscopic transitions to accompany the macroscopic morphology transitions of the interface. Thus future research must concentrate both on more measurements of such macroscopic quantities as the interface velocity and on the microscopic characterization of the interface and the bulk structure which grows.

Acknowledgements — We thank David Kessler for useful discussions, A. Ben-Jacob for her assistance, and R. Kupferman for his comments on the manuscript. This research was partially supported by NSF Grant DMR 8608305, the Israeli Academy of Science, the Tel-Aviv University Grant for Basic Research, and the Petroleum Research Fund of the American Chemical Society. We further acknowledge the NSF Office of Supercomputing for providing time on the San Diego Supercomputing Center Cray. E. Ben-Jacob is a Bat-Sheva Fellow.

References

1. E. Ben-Jacob, N.D. Goldenfeld, J.S. Langer, and G. Schön, Physical Review Letters **51**, 1930 (1983) and Physical Review **A29**, 330 (1984).
2. D.A. Kessler, J. Koplik, H. Levine, Physical Review **A30**, 3161 (1984).
3. E. Ben-Jacob, R. Godbey, N.D. Goldenfeld, J. Koplik, H. Levine, T. Mueller, and L.M. Sander, Physical Review Letters **55**, 1315 (1985).
4. T. A. Witten and L. M. Sander, Physical Review Letters **47**, 1400 (1981).
5. P. Meakin, Physical Review **A27**, 604 (1983).
6. E. Ben-Jacob, G. Deutscher, P. Garik, N.D. Goldenfeld, and Y. Lareah, Physical Review Letters **57**, 1903 (1986).
7. Y. Sawada, A. Dougherty, and J.P. Gollub, Physical Review Letters **56**, 1260 (1986).
8. D. Grier, E. Ben-Jacob, R. Clarke, and L.M. Sander, Physical Review Letters **56**, 1264 (1986).

9. V. Horvath, T. Vicsek, and J. Kertesz, *preprint.*
10. A. Buka, J. Kertesz, and T. Vicsek, Nature **323**, 424 (1986).
11. E. Ben-Jacob, P. Garik, D. Grier, and T. Mueller, *submitted for publication.*
12. E. Ben-Jacob, N.D. Goldenfeld, J.S. Langer, and G. Schön, Physical Review **A29**, 330 (1984).
13. R. Brower, D.A. Kessler, J. Koplik, and H. Levine, Physical Review Letters **51**, 1111 (1983) and Physical Review **A29**, 1335 (1984).
14. E. Ben-Jacob, N.D. Goldenfeld, B.G. Kotliar, and J.S. Langer, Physical Review Letters **53**, 2110 (1984).
15. D.A. Kessler, J. Koplik, and H. Levine, Physical Review **A31**, 1712 (1985).
16. D.A. Kessler and H. Levine, Physical Review **A33**, 7867 (1986).
17. D.I. Meiron, Physical Review **A33**, 2704 (1986).
18. Y. Saito, G. Goldbeck-Wood, H. Müller-Krumbhaar, Physical Review Letters **58**, 1541 (1987).
19. L. Paterson, Journal of Fluid Mechanics **113**, 513 (1981).
20. S.N. Rauseo, P.D. Barnes, and J.V. Maher, *preprint.*
21. G. Daccord, J. Nittmann, and H.E. Stanley, Physical Review Letters **56**, 336 (1986).
22. A. Buka and P. Palffy-Muhoray, *to be published.*
23. M. Matsushita, M. Sano, Y. Hayakawa, H. Honjo, and Y. Sawada, Physical Review Letters **53**, 286 (1984).
24. A. Miller, W. Knoll, and H. Möhwald, Physical Review Letters **56**, 2633 (1986).
25. L. Niemeyer, L. Pietronero, and H.J. Wiesmann, Physical Review Letters **57**, 650 (1986).
26. N.D. Goldenfeld, *preprint.*
27. T. Vicsek, Physical Review Letters **53**, 2281(1984).
28. L.P. Kadanoff, J. Stat. Phys. **39**, 267 (1985).
29. L.M. Sander, P. Ramanlal, and E. Ben-Jacob, Physical Review **A32**, 3160 (1985).
30. P. Garik, R. Richter, J. Hautman, and P. Ramanlal, Physical Review **A32**, 3156 (1985).
31. R.M. Brady and R.C. Ball, Nature(London) **309**, 225 (1984).
32. E. Ben-Jacob and P. Garik, *to be published.*
33. L. Paterson, Phys. Fluids **28**, 26 (1985).
34. W.W. Mullins and R.F. Sekerka, Journal of Applied Physics **34**, 323 (1963).
35. C.-W. Park and G.M. Homsy, Journal of Fluid Mechanics **139**, 291 (1984).
36. T.A. Witten and L.M. Sander, Phys. Rev. B**27**, 5686 (1983).
37. J.D. Chen and D. Wilkinson, Physical Review Letters **55**, 1892 (1985).
38. S.-K. Chan, H.-H. Reimer, and M. Kahlweit, Journal of Crystal Growth **32**, 303 (1976).
39. J. Langer, Reviews of Modern Physics **52**, 1(1980).
40. R. Wilkins, D. Grier, E. Ben-Jacob, and P. Garik, *in preparation.*